*J. Fluid Mech.* (1985), *vol.* 151, *pp.* 121–140
*Printed in Great Britain*



# Convective influence on the stability of a cylindrical solid–liquid interface

By Q. T. FANG, M. E. GLICKSMAN,
Materials Engineering Department, Rensselaer Polytechnic Institute, Troy, New York 12181

S. R. CORIELL†, G. B. McFADDEN‡ AND R. F. BOISVERT‖
National Bureau of Standards, Washington, D.C. 20234

(Received 15 November 1983 and in revised form 3 August 1984)

Experiments in which a long vertical, heated wire is surrounded by concentric annuli of a melt and its crystalline solid show that the convection state changes from a stable unicell surrounded by a stationary cylindrical solid–liquid interface, to a complex time-dependent flow surrounded by a rotating, helical solid–liquid interface. This transition occurs at a Grashof number of approximately 150, which is an order of magnitude less than the critical Grashof number calculated for a liquid annulus surrounded by rigid walls. A linear stability analysis has been carried out for an infinitely tall vertical annulus. When the deformable nature of the crystal–melt interface is taken into account in the boundary conditions, two new modes of instability arise. The most dangerous mode is asymmetrical and corresponds to helical waves travelling vertically upwards. The critical Grashof number and the scaling properties of the eigenstate agree with experiments. The results clearly demonstrate the coupling of convection with crystal–melt interfacial instabilities.

## 1. Introduction

There has been extensive research and development on the effect of fluid flow on solidification and on the properties of the resulting solids (see e.g. Hurle 1977; Carruthers 1977; Pimputkar & Ostrach 1981). Morphological instabilities have been reviewed by Langer (1980) and Wollkind (1979), and hydrodynamic instabilities by Drazin & Reid (1981). The effect of convective flow on morphological stability has been reviewed recently by Coriell & Sekerka (1981). Delves (1974) showed theoretically that a flow parallel to the crystal–melt interface could increase stability and give rise to travelling waves on the interface. The interaction of morphological instability and thermosolutal instability has also been studied by Coriell *et al.* (1980). In both these cases, morphological instability occurs even in the absence of fluid flow, although in general the critical value of the parameter for the onset of instability is changed by the flow.

A recent series of experiments (Mickalonis 1982; Glicksman & Mickalonis 1982; Fang 1983) have demonstrated a novel interface instability under conditions for which the crystal–melt interface would be morphologically stable in the absence of flow. In these experiments, a long vertical cylindrical sample of high-purity succinonitrile (SCN) was heated by an electrical current passed through a long coaxial

† Metallurgy Division. ‡ Mathematical Analysis Division.
‖ Scientific Computing Division.

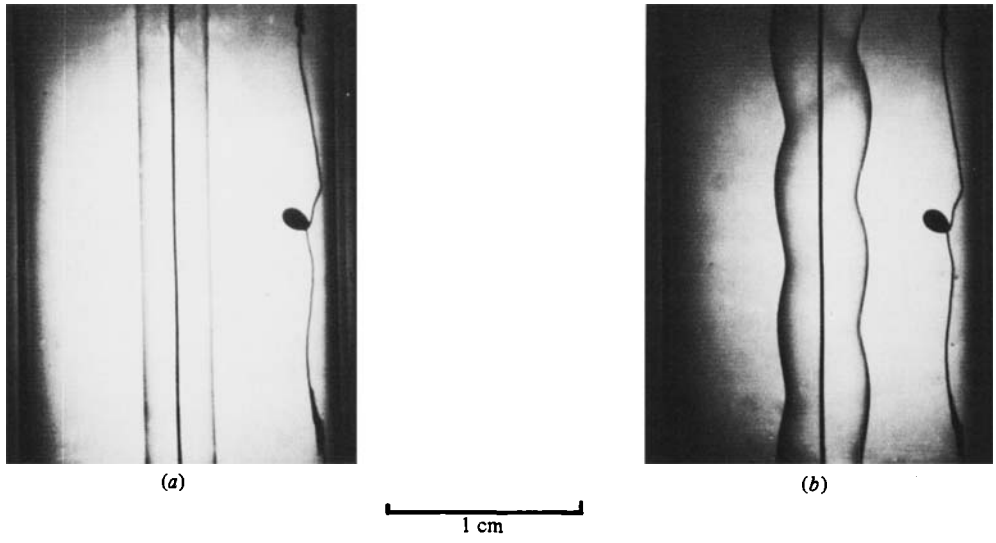


FIGURE 1. View of the stable cylindrical mode (*a*) and helical mode (*b*). The black spot on the right-hand side is the profile of a thermistor that detects temperature variations in the crystal.

heating wire, so that a vertical melt annulus formed between the coaxial heating wire and the surrounding crystal–melt interface. The outer radius of the crystal was maintained at a constant temperature below the melting point of the material. This arrangement permits the temperature to decrease monotonically from the melt to the solid across the crystal–melt interface, and consequently the interface would be morphologically stable in the absence of fluid flow (Coriell & Sekerka 1981).

The thermal gradients in the melt induce buoyancy forces which cause the fluid to flow upward near the heating wire on the axis and downward near the crystal–melt interface. Choi & Korpela (1980) assumed an infinite cylindrical geometry with rigid walls and obtained analytic solutions of the fluid-flow and temperature equations, in which the flow velocity is axial (vertical) and the velocity and temperature fields are functions of the radial coordinate alone. Choi & Korpela and Shaaban & Özisik (1982) used linear stability analysis to calculate the critical Grashof number for axisymmetric instabilities of the axisymmetric flow occurring between two vertical infinite coaxial cylinders held at different temperatures. For the Prandtl number corresponding to succinonitrile the flow is unstable to an infinitesimal axisymmetric perturbation above a Grashof number of the order of 2000, and the resulting wave speed of this perturbation is comparable to the maximum in the characteristic unperturbed flow velocity.

In contrast, as illustrated in figure 1 the experimental observations with a crystal–melt interface indicate an asymmetric instability at a critical Grashof number of about 150 with a wave speed two orders of magnitude less than the unperturbed flow velocity. Therefore we have investigated the effect of a deformable crystal–melt interface on the stability of the flow between an infinite vertical cylinder maintained at a constant temperature and a coaxial crystal–melt interface. As will be described, the presence of the crystal–melt interface leads to additional modes of instability.

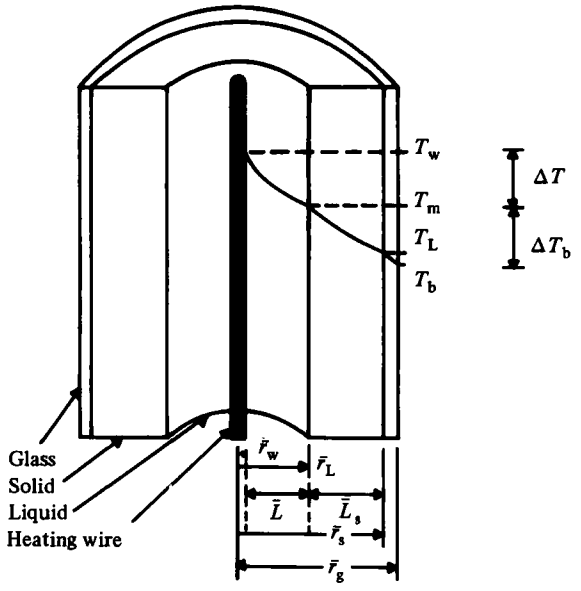


FIGURE 2. The geometric configuration and relative temperature profile of the experimental set-up. Symbols indicating radial distances imply dimensional lengths.

## 2. Linear stability analysis

### 2.1. *Theory*

The unperturbed cylindrical melt is assumed to occupy the region $\bar{r}_w \leqslant \bar{r} \leqslant \bar{r}_L$, $-\infty \leqslant \bar{z} \leqslant \infty$, in cylindrical coordinates as shown in figure 2. Here $\bar{r}_w$ is the wire radius, $\bar{r}_L$ is the radius of the solid–liquid interface, and the outer radius of the crystal is $\bar{r}_L + \bar{L}_s$. A bar will be used to distinguish dimensional quantities from dimensionless quantities where necessary. The aspect ratio of height to radius for the container used in the experiment was about 20. For Grashof numbers less than about 150 the unperturbed flow near the midsection of the tube appears to be parallel. The fluid flow will be described by the Navier–Stokes equations in the Oberbeck–Boussinesq approximation, with constant kinematic viscosity $\nu$, coefficient of thermal expansion $\beta$ and thermal diffusivity $\alpha_L$. The unit of length is chosen to be $\bar{L} = \bar{r}_L - \bar{r}_w$. Time is measured in units of $\bar{L}^2/\nu$, and velocity is measured in units of $\bar{g}\beta\bar{L}^2\Delta T/\nu$. The acceleration due to gravity $\bar{g}$ points in the negative $z$-direction. Temperature is measured in units of $\Delta T$, the temperature difference between the wire and the solid–liquid interface; the origin of the dimensionless temperature scale is chosen so that the melting point of a planar crystal–melt interface is zero.

The dimensionless equations governing the stability of the unperturbed flow are

$$\nabla \cdot \boldsymbol{u} = 0, \tag{1}$$

$$\frac{\partial \boldsymbol{u}}{\partial t} + G(\boldsymbol{u}\cdot\nabla)\,\boldsymbol{u} + \nabla p = T\hat{\boldsymbol{z}} + \nabla^2 \boldsymbol{u}, \tag{2}$$

$$\frac{\partial T}{\partial t} + G(\boldsymbol{u}\cdot\nabla)\,T = \frac{\nabla^2 T}{P_r}, \tag{3}$$

$$\frac{\partial T_s}{\partial t} = \frac{\nabla^2 T_s}{P_{rs}}, \tag{4}$$

where the Grashof number $G = \beta \bar{g} \Delta T \bar{L}^3/\nu^2$, the Prandtl number $P_r = \nu/\alpha_L$ and $P_{rs} = \nu/\alpha_s$, with $\alpha_s$ the thermal diffusivity of the crystal. The velocity $\boldsymbol{u} = (u_r, u_\phi, u_z)$, $p$ is the reduced pressure, and $T$ and $T_s$ are the temperature in the liquid and solid respectively.

The unperturbed velocity, derived by Choi & Korpela (1980), is given by

$$\begin{aligned} \boldsymbol{u}_0 &= u_{z0}(r)\,\boldsymbol{z} \\ &= \boldsymbol{z}\left\{C\left[\rho^2 - 1 + (1-\kappa^2)\frac{\ln\rho}{\ln\kappa}\right] - 4(\rho^2-\kappa^2)\frac{\ln\rho}{\ln\kappa}\right\}\Big/[16(1-\kappa)^2], \end{aligned} \tag{5}$$

with

$$\kappa = \bar{r}_w/\bar{r}_L, \quad \rho = (1-\kappa)\,r$$

and

$$C = [(1-\kappa^2)(1-3\kappa^2) - 4\kappa^4 \ln\kappa]/[(1-\kappa^2)^2 + (1-\kappa^4)\ln\kappa].$$

The unperturbed velocity vanishes at the inner cylinder $r = \kappa/(1-\kappa)$ and at the unperturbed crystal–melt interface $r = 1/(1-\kappa)$. In addition, the net flow vanishes; the integral of $ru_{z0}(r)$ from $r = \kappa/(1-\kappa)$ to $r = 1/(1-\kappa)$ is zero. The unperturbed temperature fields are given by

$$T_0(r) = T_e + \ln\rho/\ln\kappa \tag{6}$$

and

$$T_{s0}(r) = T_e + \frac{K_L}{K_s}\frac{\ln\rho}{\ln\kappa}, \tag{7}$$

where $T_e$ is the dimensionless equilibrium temperature of the unperturbed crystal–melt interface, and $K_L$ and $K_s$ are thermal conductivities of liquid and crystal respectively. The unperturbed crystal is neither freezing nor melting. Thus for a given cylindrical geometry, characterized by $\kappa$, there is a family of parallel flows with dimensional velocities proportional to the Grashof number. The parallel flow becomes unstable for large enough Grashof number.

We decompose the fluid velocities, temperature fields and crystal–melt interface shape $r = R(\phi, z, t)$ into unperturbed and perturbed parts, and assume that the $\phi$-, $z$-, $t$-dependences of the perturbed quantities are of the form

$$F(\phi, z, t) = \exp(in\phi + ikz + \sigma t),$$

where $n$ is an integer, $k$ is a real spatial frequency, and $\sigma = \sigma_r + i\sigma_i$ is complex and determines the temporal behaviour of the system. If $\sigma_r > 0$ for any value of $n$ and $k$, the system is unstable. We write

$$u_r = W_r(r)\,F, \quad u_\phi = W_\phi(r)\,F, \quad u_z = u_{z0}(r) + W_z(r)\,F, \tag{8a–c}$$

$$T = T_0(r) + \theta(r)\,F, \quad T_s = T_{s0}(r) + \theta_s(r)\,F \quad \text{and} \quad r_I = 1/(1-\kappa) + aF. \tag{8d–f}$$

Here $a$ is the amplitude of the perturbation of the solid–liquid interface. The linearized ordinary differential equations for the perturbed quantities are standard and are given in Coriell *et al.* (1983).

The boundary conditions at the inner cylinder (heating wire) are the usual statements of 'no slip' and 'no normal flow'; also, we assume that the temperature perturbation vanishes. Thus at $r = \bar{r}_w/\bar{L} = \kappa/(1-\kappa)$

$$W_z = W_r = W_\phi = \theta = 0. \tag{9}$$

Similarly, we assume that a perturbation in temperature does not occur at the outer wall of the solid.

The interface separating the crystal and melt is a free boundary; the solidification boundary conditions (see e.g. Wollkind 1979; Coriell & Sekerka 1981) at this interface

are crucial in explaining the observed phenomena. The dimensionless boundary conditions at the crystal–melt interface $r = R(\phi, z, t)$ are

$$T = T_s = -\frac{\gamma}{G} H(\phi, z, t), \tag{10a}$$

$$A(\boldsymbol{v}\cdot\boldsymbol{n}) = \left[\nabla T_s - \frac{K_L}{K_s}\nabla T\right]\cdot\boldsymbol{n}, \tag{10b}$$

$$\boldsymbol{u}\cdot\boldsymbol{n} = -\epsilon(\boldsymbol{v}\cdot\boldsymbol{n}), \tag{10c}$$

together with the no-slip condition, i.e. the tangential components of $\boldsymbol{u}$ vanish. Equation (10$a$) expresses that the temperature at the crystal–melt interface is continuous and is equal to the equilibrium interfacial temperature, which depends on the mean curvature $H$ of the interface through the Gibbs–Thomson effect (Mullins 1963; Wollkind 1979). Equilibrium thermodynamics implies that the sign of the curvature should be chosen such that a crystalline sphere has positive curvature and a liquid sphere has negative curvature. The dimensionless surface tension $\gamma = \bar{T}_m \bar{\gamma}\bar{g}\bar{\beta}\bar{L}^2/(H_v \nu^2)$, where $\bar{T}_m$ is the absolute temperature at the melting point for a planar interface, $\bar{\gamma}$ is the crystal–melt interface tension and $H_v$ is the latent heat of fusion per unit volume of solid. The Gibbs–Thompson equation (10$a$) is the basis of the 'grain boundary groove method' of measuring the crystal–melt interface tension, and has been applied to succinonitrile by Schaefer, Glicksman & Ayers (1975). Equation (10$b$) expresses conservation of energy at the interface; the latent heat generated by motion of the interface at velocity $\boldsymbol{v}$ is balanced by the net heat flux. The unit normal to the interface is denoted by $\boldsymbol{n}$ and the dimensionless latent heat $A = H_v \bar{g}\bar{\beta}\bar{L}^3/K_s \nu$. Conservation of mass at a moving crystal–melt interface requires a non-zero flow normal to the interface when the densities $\rho_s$ and $\rho_L$ of the solid and liquid respectively are unequal. This is expressed by (10$c$), where $\epsilon = (\rho_s/\rho_L) - 1$. Note that during crystal growth, material penetrates the crystal–melt interface, which is therefore not a 'material surface', for which the fluid velocity normal to the surface is equal to the normal velocity of the surface.

Upon linearizing the solidification boundary conditions about the unperturbed solid–liquid interface at $r_{I0} = 1/(1-\kappa)$, the following linear homogeneous boundary conditions can be obtained:

$$a_1 W_r + \epsilon\sigma\theta = 0, \tag{11}$$

$$W_\phi = 0, \tag{12}$$

$$a_1 W_z + (\mathrm{D}u_{z0})\, G\theta = 0, \tag{13}$$

$$-a_2\theta + a_1 \frac{K_L}{K_s}\mathrm{D}\theta = 0. \tag{14}$$

Here

$$\mathrm{D} = \frac{\partial}{\partial r},\quad a_1 = \gamma\left[\frac{n^2-1}{r_{I0}^2} + k^2\right] - G\,\mathrm{D}T_0 \quad \text{and} \quad a_2 = \frac{\mathrm{D}\theta_s}{\theta_s}\left[a_1 + G(\mathrm{D}T_0)\left(1 - \frac{K_L}{K_s}\right)\right] - A\sigma.$$

The ratio $(\mathrm{D}\theta_s)/\theta_s$ evaluated at $r_{I0}$ that appears in the expression for $a_2$ can be expressed in terms of Bessel functions. The interface perturbation amplitude $a$ is given by

$$a = -W_z/\mathrm{D}u_{z0},$$

at $r = r_{I0}$.

The thermal properties of the liquid and solid phases of the test substance, succinonitrile, are approximately equal, i.e. $K_L = K_s$ and $P_r = P_{rs}$. Furthermore,

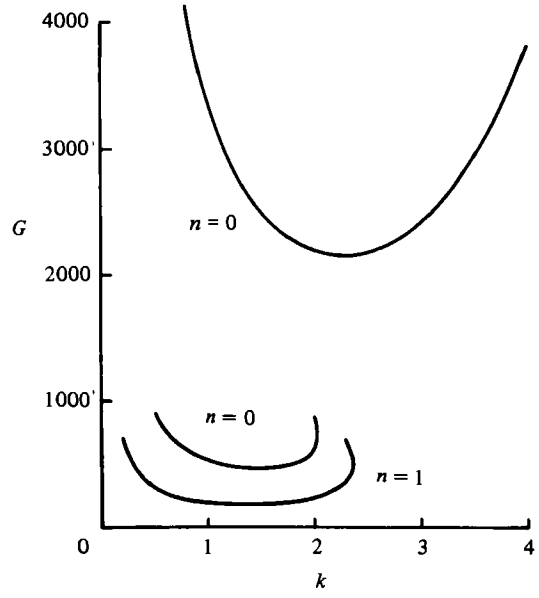


FIGURE 3. The Grashof number $G$ at the onset of instability as a function of the spatial frequency $k$ of a sinusoidal perturbation. The lowest two modes occur only for a crystal–melt interface, while the highest mode occurs for both a crystal–melt interface and a rigid interface.

numerical calculations indicate that the effects of the crystal–melt surface tension and the density change upon solidification are not important. Thus, setting $K_L = K_s$, $\epsilon = 0$ and $\gamma = 0$, the boundary conditions (11)–(14) reduce to

$$W_r = W_\phi = 0, \tag{15}$$

$$-(DT_0')\, W_z + (Du_{z0})\,\theta = 0 \tag{16}$$

and

$$\left[\frac{D\theta_s}{\theta_s} + \frac{\Lambda\sigma}{G(DT_0')}\right]\theta - D\theta = 0. \tag{17}$$

It is interesting to point out here that, if $D\theta$ appearing in (17) is negligible, then the above boundary conditions become $W_r = W_\phi = W_z = \theta = 0$, which are identical with those for rigid boundaries.

The numerical methods used to solve the linear eigenvalue problem are similar to those previously described (Coriell *et al.* 1980). We fixed $\sigma_r$ and varied $G$ and $\sigma_i$, keeping the remaining parameters constant, until a solution was found of the differential equations satisfying the boundary conditions. The program SUPORT (Scott & Watts 1977) was used to solve the differential equations, and the program SNSQE (SLATEC Common Math Library, National Energy Software Center, Argonne National Lab., Argonne, IL, written by K. L. Hiebert, based on Powell 1970) was used for the nonlinear iteration procedure. For the case of rigid boundaries, we have compared our results for $G$ and $\sigma_i$ with $n = 0$ and $P_r = 15$ with those of table 1 of Choi & Korpela (1980), who used different numerical methods. We obtained agreement to about 1 %.

### 2.2. *Numerical results and theoretical predictions*

Figure 3 displays the critical Grashof number ($\sigma_r = 0$) as a function of the spatial frequency for three different modes. The parameters used are $P_r = P_{rs} = 22.8$, $\epsilon = 0.0283$, $\gamma = 4.53 \times 10^{-4}$, $\Lambda = 1.017 \times 10^4$, $K_L/K_s = 1.0$, $\kappa = 0.02$ and $\bar{L}_s/\bar{L} = 1.0$

| Property | Symbol | Value† |
|---|---|---|
| Density of solid | $\rho_s$ | 1.016 g cm$^{-3}$‡ |
| Density of liquid | $\rho_L$ | 0.988 g cm$^{-3}$‡ |
| Thermal expansivity (solid) | $\beta_s$ | $5.6 \times 10^{-4}$ K$^{-1}$ |
| Thermal expansivity (liquid) | $\beta$ | $8.1 \times 10^{-4}$ K$^{-1}$ |
| Kinematic viscosity | $\nu$ | $2.6 \times 10^{-2}$ cm$^2$ s$^{-1}$ |
| Triple-point temperature | $T_p$ | 331.23 K |
| Latent heat of fusion | $H_v$ | 47.8 J cm$^{-3}$ |
| Surface tension (solid–liquid) | $\bar{\gamma}$ | $8.94 \times 10^{-7}$ J/cm$^2$ |
| Heat capacity of solid | $C_{ps}$ | 1.913 J g$^{-1}$ K$^{-1}$‡ |
| Heat capacity of liquid | $C_{pL}$ | 2.000 J g$^{-1}$ K$^{-1}$‡ |
| Thermal conductivity (solid) | $K_s$ | $2.25 \times 10^{-3}$ J cm$^{-1}$ K$^{-1}$ s$^{-1}$‡ |
| Thermal conductivity (liquid) | $K_L$ | $2.23 \times 10^{-3}$ J cm$^{-1}$ K$^{-1}$ s$^{-1}$‡ |
| Thermal diffusivity (solid) | $\alpha_s$ | $1.16 \times 10^{-3}$ cm$^2$ s$^{-1}$‡ |
| Thermal diffusivity (liquid) | $\alpha_L$ | $1.12 \times 10^{-3}$ cm$^2$ s$^{-1}$‡ |

† A detailed source of these data can be found in Glicksman, Schaefer & Ayers (1976).
‡ Indicates value of property at melting point.

TABLE 1. Properties of succinonitrile

(a list of some physical constants is given in table 1). The lowest and most 'dangerous' mode is asymmetric, with a minimum at $k = 1.35$, $G = 176$, and $\sigma_i = -0.977 \times 10^{-2}$. The lower symmetric mode ($n = 0$) has a minimum at $k = 1.45$, $G = 464$ and $\sigma_i = -3.65 \times 10^{-2}$, whereas the higher symmetric mode has a minimum at $k = 2.3$, $G = 2152$ and $\sigma_i = -43.7$. With the assumption that $\epsilon = \gamma = 0$, the values of $G$ and $\sigma_i$ change by less than 0.1 %. Similarly, the results are insensitive to the form of the thermal boundary condition at the wire, e.g. changing from Dirichlet to Neumann conditions changes the critical Grashof number by about 0.5 %.

The higher symmetric mode in figure 3 is virtually identical with that obtained if the crystal–melt interface is replaced by a rigid isothermal boundary, i.e. replace the crystal–melt boundary conditions (11)–(14) or (15)–(17) with (9). For this mode, in fact, the factor multiplying $\theta$ in (17) is very large compared with unity, and $\theta \approx 0$ at the crystal–melt boundary. There is little interface deformation in this mode. The lower axisymmetric and the asymmetric mode by contrast occur only when a compliant crystal–melt boundary is present. The magnitude of the coefficient of $\theta$ in (17) for these two modes is of order unity; $\theta$ and $D\theta$ become of the same order of magnitude.

The higher symmetric mode may be denoted as a 'convective mode', since it involves little interface deformation and is similar to the mode that occurs at this Prandtl number when a rigid boundary is present. In that case, the disturbance takes the form of a travelling wave ($\sigma_i \neq 0$) in the positive $z$-direction. The mechanism for instability is an energy transfer from the main flow to the disturbance due to the buoyancy force (Choi & Korpela 1980). The lower symmetric and the asymmetric mode, which occur only in the presence of fluid flow and a crystal–melt interface, will be denoted as 'coupled modes'. The wave speed for the convective mode is approximately the same as the maximum flow velocity, whereas the wave speeds for the coupled modes are about two orders of magnitude smaller than the maximum flow velocity. Apparently the crystal–melt transformation, which involves both melting and freezing with latent-heat absorption and release, can only follow the relatively slow fluid motions of the coupled mode.

The dependence of $G$ and $\sigma_i$ on $k$ for the lowest mode is shown in more detail in

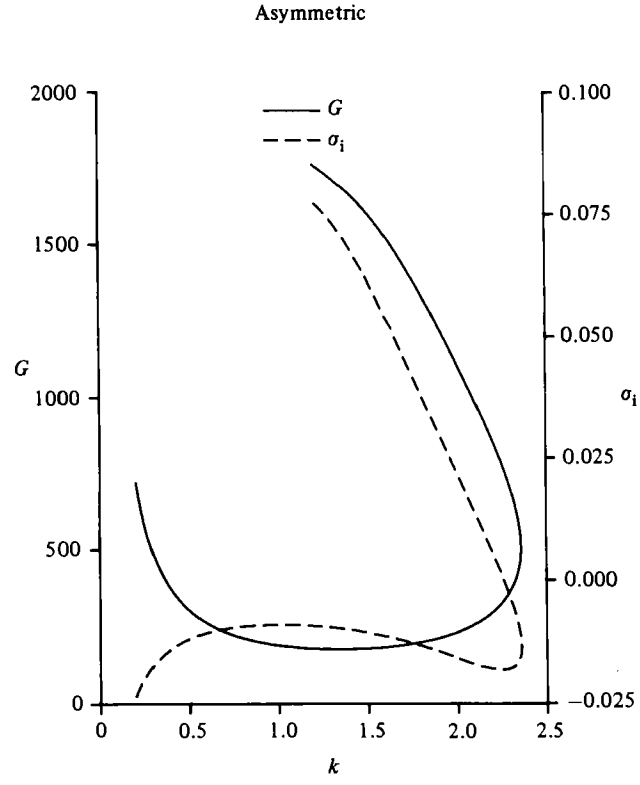


FIGURE 4. Dependence of $G$ and $\sigma_i$ for the lowest mode ($n = 1$), with $P_r = 22.8$ and $\kappa = 0.02$.

figure 4. In this case the disturbance travels upward ($\sigma_i < 0$) at the minimum Grashof number, although $\sigma_i$ becomes positive for larger Grashof numbers on this branch. With $n = 1$ ($n = -1$), the disturbance has the form of a rotating left-handed (right-handed) helix.

## 3. Experimental apparatus and procedures

### 3.1. *Apparatus*

The experimental apparatus consisted of a constant-temperature bath, temperature-control devices, observation tubes and a camera. The constant-temperature bath contained a mixture of ethylene glycol and distilled water. The volume of the constant-temperature bath was about 30 litres, and the heat-transfer fluid was kept homogeneous in temperature by a stirring motor. The temperature was regulated by a temperature-control system.

The tank temperature was monitored with a platinum resistance thermometer and a null detector in combination with a thermometer bridge (Smith bridge). The thermometer's resolution is 0.0004 K, and the bridge's resolution is 0.000 01 Ω. The temperature stability of the tank fluid after steady state was established was better than ±0.0005 K within a day. The specimen tube was viewed with a stereomicroscope through a 10 × 12 cm plateglass window located in the front side of the tank wall.

The details of the specimen tube are shown in figure 5. The axial heating wire was platinum, 0.0203 cm in diameter. This wire was soldered to copper current leads at

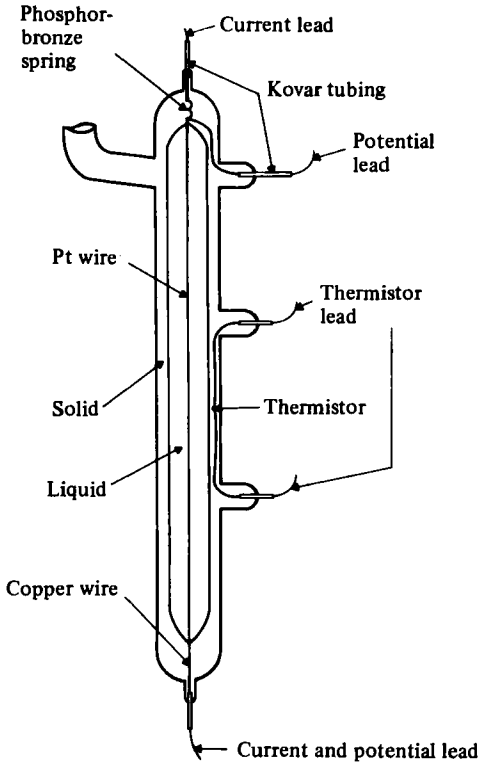


FIGURE 5. Geometric configuration of the main experimental tube.

both ends, with a phosphor-bronze spring provided at the top end to maintain tension.

The platinum wire served a dual purpose. First, it provided the heat-generating source needed to keep the tube axis above the melting temperature of the test substance, succinonitrile. Secondly, it served as a thermometer through the variation of its resistance with temperature.

### 3.2. *Determination of the critically unstable state*

When the temperature difference between the wire and the bath was increased sufficiently, an initially cylindrical solid–liquid interface transformed into a rotating helical interface. This new state was observed to persist, with a well-defined rotation period and amplitude of interfacial deformation.

It was observed that the base flow is vertical and laminar when the Grashof number is smaller than the critical value, except in the region 2–3 cm near the top and bottom, where the turning flows occur. This was confirmed by examining the trajectories of inert and density-matched particles which were introduced into the sample. When the Grashof number exceeded the critical value, then the particle trajectories became complex, indicating a change in the base flow pattern. The observed wavelength of the helical disturbance is small compared with the length of the cylinder.

### 3.3. *Measurement of helical-wave rotation period*

We employed three methods to measure the period of rotation. The first was the 'thermistor method'. As the helical interface rotates it creates a periodic thermal field

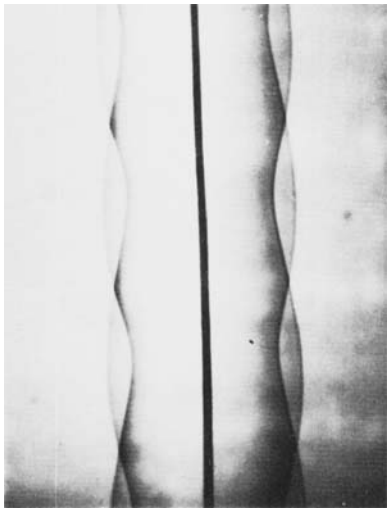


(*a*)

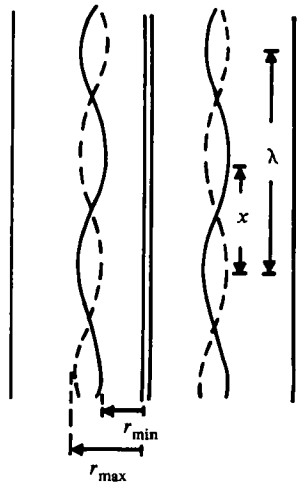


(*b*)

FIGURE 6. Sequential photographic records of crystal–melt interface movement (*a*) and the corresponding schematic plot (*b*).

in the solid region. The period of the temperature variation at any given point in the solid region is the same as that of the rotating interface. Consequently, the period can be measured with a thermistor imbedded in the solid region.

The second method of measuring the rotation period employed photographic methods. Since the profile of the solid–liquid interface gave a sharp image on a photograph, a sequence of photographs would register the progressive movement of the interface. The period may then be determined as

$$t_p = \Delta t(\lambda/\Delta x), \tag{18}$$

where $\Delta t$ and $\Delta x$ are respectively the time interval and the corresponding displacement between two consecutive photographs, and $\lambda$ is the wavelength of the interface helix as shown in figure 6.

For measuring long-period waves the thermistor technique had a distinct advantage because it is easily automated. Typical uncertainty of the measured data in these periods was about $\pm 2\,\%$. However, for helix rotation periods under about 30 min, the photographic method is more satisfactory.

The rotation period could also be determined by measuring the time required for a wave peak to travel past two fixed reference points on a scaled lens. For periods less than about twenty minutes, this method proved to be extremely accurate and convenient, yielding uncertainties within $\pm 1\,\%$.

The radial gap of the liquid region was determined from photographs of the interface at the midsection of the fluid-flow chamber by measuring the average distance of the interface from the central heating wire; that is,

$$\bar{L} = \tfrac{1}{2}(\bar{r}_{max} + \bar{r}_{min}) - \bar{r}_w, \tag{19}$$

where $\bar{L}$ is the average liquid radial gap, and $\bar{r}_{max}$ and $\bar{r}_{min}$ are the maximum and minimum radii of the interface wave.

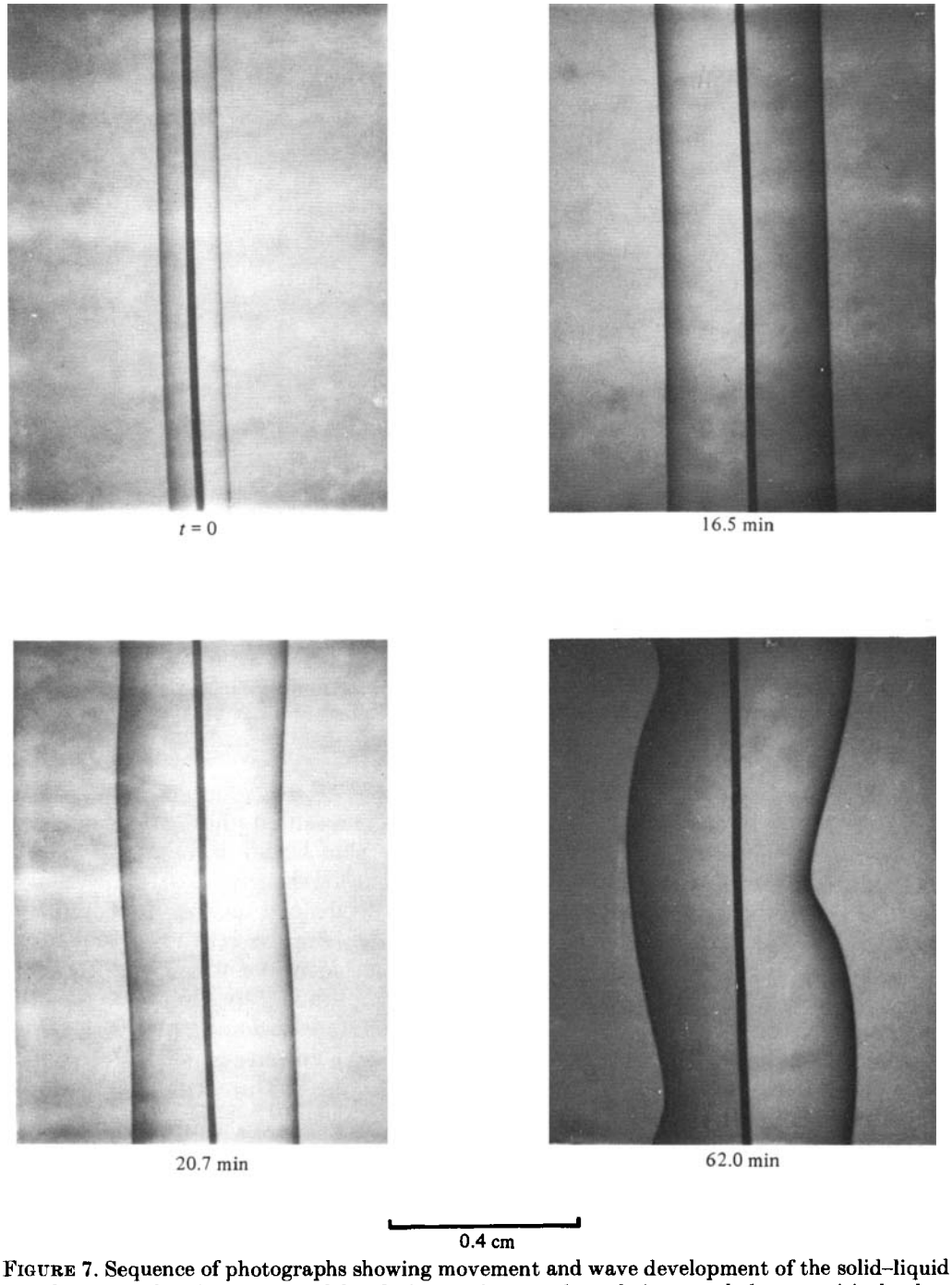


FIGURE 7. Sequence of photographs showing movement and wave development of the solid–liquid interface as the heating current of the platinum wire was abruptly increased above a critical value. Bath temperature was 37 °C.

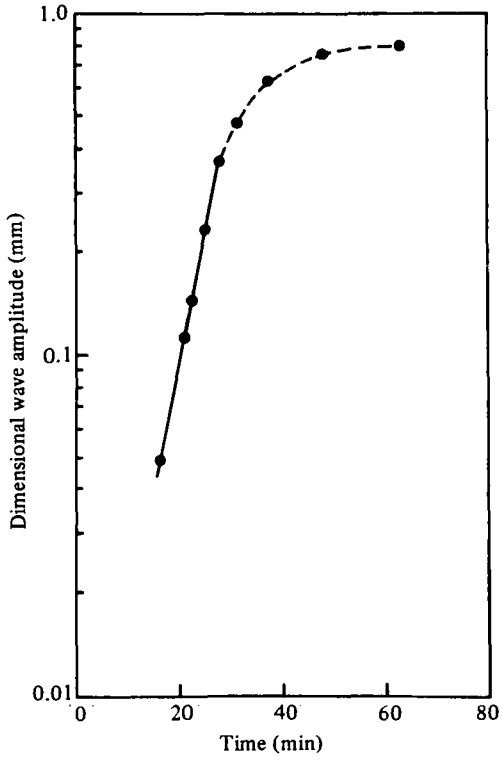


FIGURE 8. The dimensional wave amplitude of the growing interface instability shown in figure 7 as a function of time. The bath temperature was 37 °C.

### 3.4. *Growth-rate measurement*

The growth rate of the helical wave amplitude was measured photographically. All these measurements were made with an initially thin liquid annulus around the heating wire. A step increase of current sufficient to exceed the critical Grashof-number condition was then applied. The wave amplitude, defined as $\frac{1}{2}(\bar{r}_{\max}-\bar{r}_{\min})$, was recorded through a series of photographs taken at appropriate time sequences. Typical photographs and the corresponding measurements of wave amplitude are shown in figures 7 and 8 respectively. The wave amplitude grows in an exponential fashion (solid line), and finally levels off in the later stage owing to nonlinear effects (broken line). The time constant of growth of the wave amplitude, $\bar{\sigma}_r$, is determined from the slope corresponding to the linear range of figure 8. The accuracy of the data reported in figure 8 (and subsequent plots) may be taken as less than the size of the datum symbol displayed.

### 3.5. *Measurement of wave helicity*

It was observed that the helix associated with interface instability may have either a right- or a left-handed sense. The helicity can be observed easily by rotating the tube slightly in the tank. Alternatively, it can be determined by decreasing the heating-wire current abruptly, thus creating a dendritic or cellular interface, which can be recorded photographically. Figure 9 shows a photograph of such a dendritic surface. We observed that a rough dendritic 'belt' formed helically on the convex freezing surface of the helix. Note that in figure 9 the fine-scale features of the 'belt'

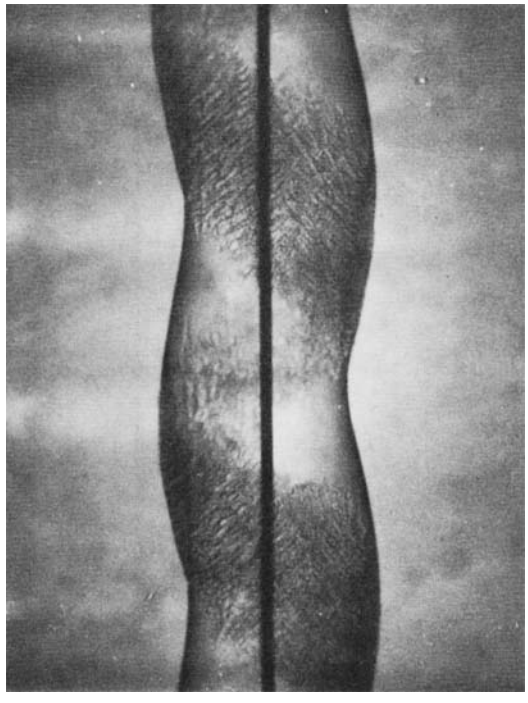


FIGURE 9. A dendritic 'belt', formed by abrupt undercooling, showing a left-handed helical crystal–melt interface.

are in sharp focus on the portions of the helix nearest the observer. By tracing the rotation of the 'belt' we ascertained the helicity of the interface, i.e. whether it was right-handed or left-handed.

## 4. Experimental results and discussion

For a given radial gap $\bar{L}$ there is a critical temperature difference for which the cylindrical state is first unstable. The critical temperature difference and certain properties of the disturbed state vary as the liquid gap is changed. Experiments were performed for different values of $\bar{L}$ to examine this dependence, and the results are described below.

### 4.1. *Scaling of the rotation period, wave-amplitude growth rate, wavelength and wave speed with respect to the average liquid radial gap*

It is noted that there is always a slight temperature gradient along the tube due to end effects. As a result, the helical deformation associated with instability tapers down the tube. For convenience we have consistently chosen a final state in which the helix disappears two-thirds of the way down the tube, and then measured various quantities near the middle section of the tube.

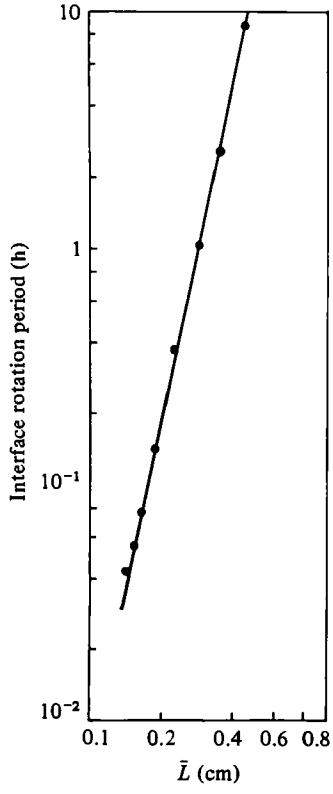


FIGURE 10

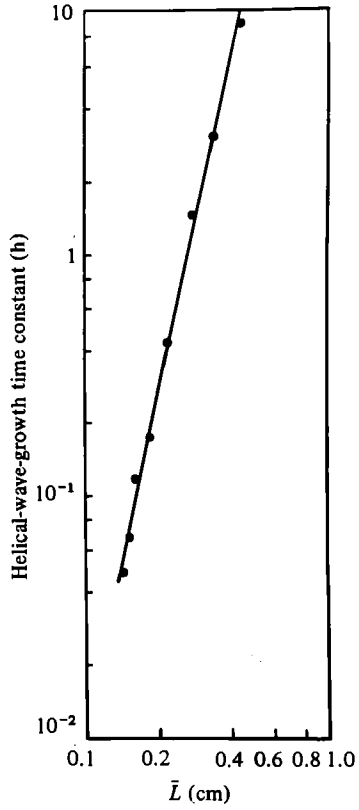


FIGURE 11

FIGURE 10. The rotation period of the helical crystal–melt interface as a function of the average liquid radial gap.

FIGURE 11. The helical-wave-growth time constant as a function of the average radial gap of the liquid.

Figure 10 shows the observed rotation period $t_p$ in the final state as a function of the average radial gap $\bar{L}$ in the liquid on a log–log plot. The slope of this curve was found to be 4.82 (as discussed below, the linear stability analysis of the marginal state predicted a value of 5.0.)

The growth rates of the wave amplitude were found to depend on the initial radial gap present in the liquid prior to the step increase in current (Fang 1983). Note that this initial gap is determined by the temperature of the coaxial heating wire for a given bath temperature, or equivalently is determined by the current passing through the wire. Preliminary experiments were performed to obtain an estimate for the value of the wire current necessary to obtain the desired final state. The initial wire current was then fixed at 70% of the final value in order to produce systematic measurements.

In principle, the change from the cylindrical mode to the helical mode could be accomplished without changing $\bar{L}$ by simultaneously increasing $T_w$ and decreasing $T_b$ by appropriate amounts. In practice, however, for a given experiment $T_w$ was increased and $T_b$ was held constant. This results in the melting back of the crystalline annulus and an increase in $\bar{L}$. This time-dependent change in $\bar{L}$ is not considered in the theoretical analysis described above. In comparing experiment and theory we have used the measured $\bar{L}$ of the helical state.

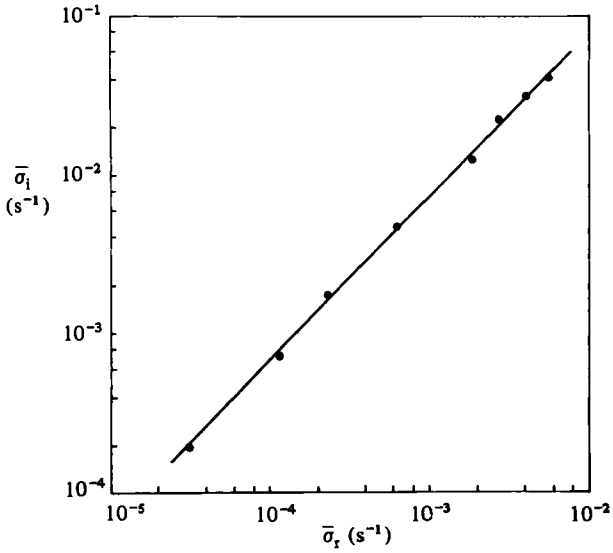


FIGURE 12. The imaginary part *vs.* the real part of the eigenvalue.

Figure 11 shows the measured radial wave-growth time constant $t_g = 1/\bar{\sigma}_r$ as a function of the average radial gap. A log–log fit to these data with a slope of 4.76 was found through least-square regression. It appears that with the chosen final conditions $t_g$ has almost the same scaling as does $t_p$ with respect to the liquid radial gap $\bar{L}$. The relation between $\bar{\sigma}_i = 2\pi/t_p$ and $\bar{\sigma}_r$ is shown in figure 12. As we see from this figure, a linear relationship is found with a slope close to unity, indicating that $\bar{\sigma}_r$ is proportional to $\bar{\sigma}_i$, or equivalently that the dimensional wave-growth time constant is proportional to the dimensional rotation period.

Figure 13 shows the measured wavelength $\lambda$ as a function of the average liquid radial gap $\bar{L}$. A linear relation exists between them with a slope of about 1.04.

The axial wave velocity, defined as the wavelength divided by the rotation period $t_p$, is shown in figure 14, as a function of the average liquid radial gap. A slope of $-3.67$ is found from these data through linear regression analysis.

We show in figure 15 the measured Grashof number in the final state as a function of $\Delta T_b$, defined as the difference between the melting point of SCN (taken as 58.08 °C) and the bath temperature. As we see in figure 15, the Grashof numbers are relatively constant, decreasing only slightly as $\Delta T_b$ is increased from 0 to 30 K.

We have carried out another series of experiments to obtain a value for the critical Grashof number. These experiments are done by keeping the bath temperature $T_b$ and the initial wire temperature $T_w$ (and thus the initial melt gap) fixed, and then varying the final wire temperature by adjusting the wire current. The results are shown in figure 16. We extrapolated the curve and obtained a critical Grashof number of 141.8, which is surprisingly close to the theoretically calculated value of 140.2. We observed that the growth rate is proportional to $G-G^*$ for $G-G^* \leqslant 20$, which is consistent with numerical calculations. However, the theoretical proportionality constant is about 50 % larger than the experimental value.

### 4.2. *Comparison with theoretical calculations and discussion*

A summary of the current experimental data and corresponding theoretical linear stability calculations is given in table 2. The calculated values are denoted by an asterisk. In these calculations it is assumed that $\epsilon = \gamma = \sigma_r = 0$, $P_r = P_{rs} = 22.8$,

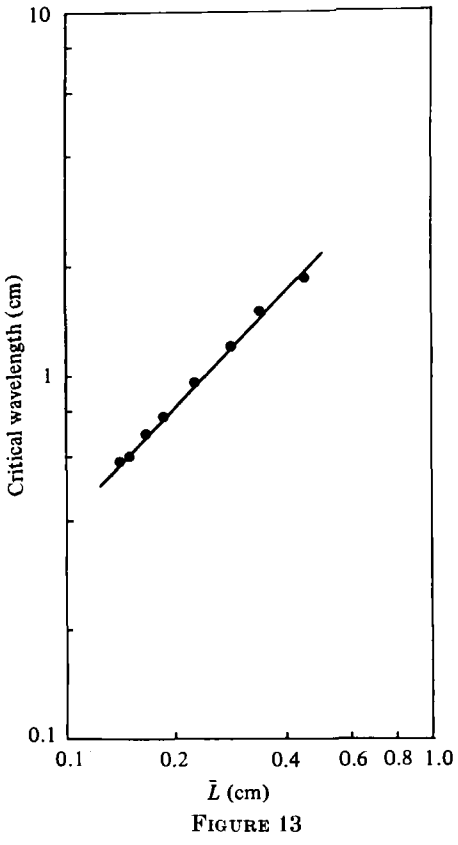


FIGURE 13

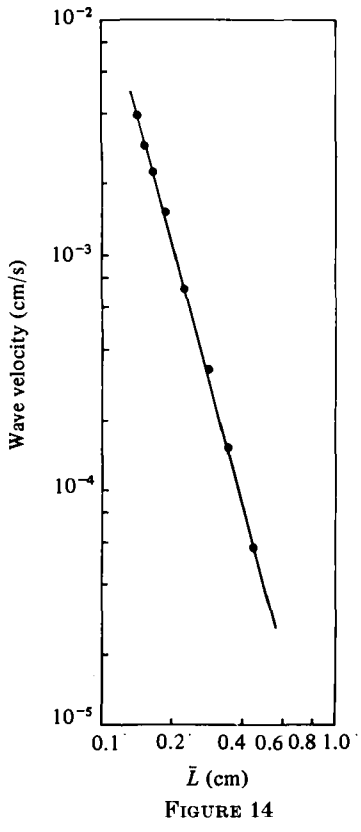


FIGURE 14

FIGURE 13. The critical wavelength as a function of the average radial gap of the liquid.

FIGURE 14. The wave velocity as a function of the average radial gap of the liquid.

$K_L/K_s = 1$, $T_m = 58.08$ °C and $n = 1$ (for asymmetric instability). The data required for these calculations are the radii $\bar{r}_w$, $\bar{r}_L$ and $\bar{r}_L + \bar{L}_s$. Comparison between experimental values and those by numerical calculations reveals the following.

(1) The experimental values of $\bar{\sigma}_i$ are systematically smaller than the calculated values by 10–45 %, and these differences become smaller as the liquid gap becomes larger. It is important to recognize that the value of $\bar{\sigma}_i$ and $\bar{L}$ are measured for the fully developed waves, and thus may be subject to nonlinear effects which are not included in the linear perturbation theory.

(2) The theoretical growth rate $\bar{\sigma}_r^*$ near marginal stability is proportional to the difference $G - G^*$ between the Grashof number and the critical Grashof number. We note that the values $\bar{\sigma}_r$ shown in table 2 correspond to the initial portion of the wave development. We have also calculated Grashof numbers based on the measured values of $\bar{\sigma}_r$ given in table 2; these results indicate that all the experiments were conducted at Grashof numbers ranging from 8 to 11 % above the Grashof number $G^*$ corresponding to marginal stability ($\bar{\sigma}_r = 0$).

(3) Experimental and theoretical values of the dimensionless wavenumber $k$ are also given in table 2. The measured values are, in general, higher than the calculated values by about 10–20 %. It is interesting to note that, despite this difference, both sets of data show systematically that the dimensionless values $k$ and $k^*$ are relatively

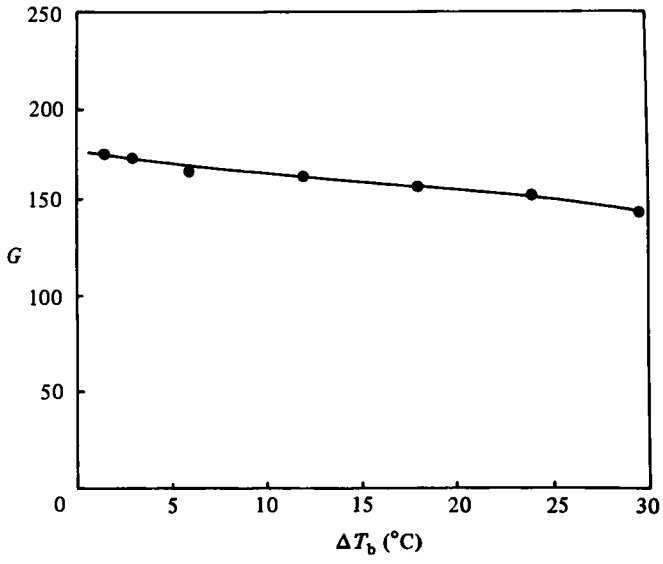


FIGURE 15. The critical Grashof number $G$ as a function of the temperature difference $\Delta T_b$ between the melting point and the bath temperature.

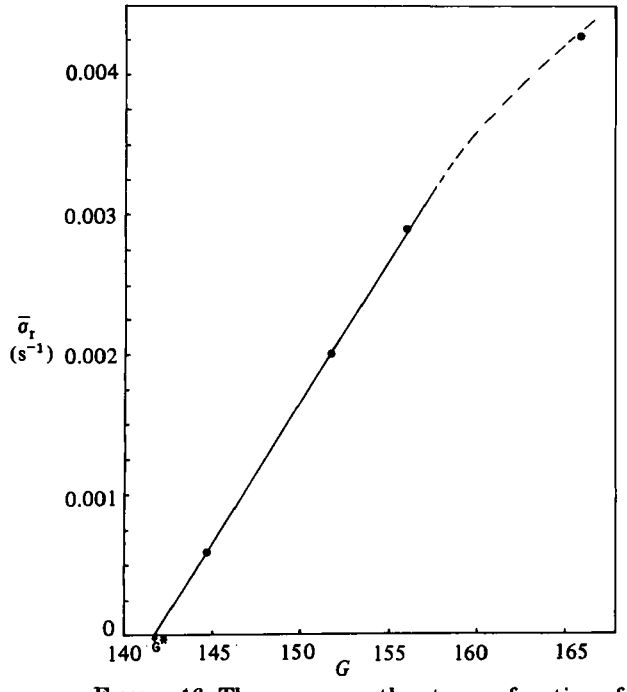


FIGURE 16. The wave growth rate as a function of $G$.

constant as $\bar{L}$ varies from about 0.14 to 0.46 cm. It is this behaviour that indicates that the dimensional wavelength is essentially proportional to the liquid gap.

(4) The predicted and measured critical Grashof numbers agree with each other in general. Moreover, both the experimental data and the theoretical calculations show that the critical Grashof numbers depend weakly on $\bar{L}$.

| $T_b$ (C) | $T_w$ (C) | $\bar{L}/\bar{L}^*$ (cm) | $\kappa$ | $\bar{\sigma}_i$ ($s^{-1}$)/$\bar{\sigma}_i^*$ ($s^{-1}$) | $\bar{\sigma}_r$ ($s^{-1}$) | $\lambda$ (cm) | $k/k^*$ | $G/G^*$ | $Q/Q^*$ | $v$ (cm/s) | $\frac{1}{2}\Delta r$ (cm) |
|---|---|---|---|---|---|---|---|---|---|---|---|
| 28.50 | 100.65 | 0.142/0.126 | 0.0666 | $4.10\times10^{-2}/5.84\times10^{-2}$ | $5.66\times10^{-3}$ | 0.586 | 1.47/1.15 | 144/140 | 60.0/85.5 | $3.82\times10^{-3}$ | 0.0189 |
| | | (−11.3) | | (+42.4) | | | (−21.8) | (−2.78) | (+42.5) | | |
| 34.00 | 95.12 | 0.152/0.136 | 0.0627 | $3.14\times10^{-2}/4.37\times10^{-2}$ | $4.07\times10^{-3}$ | 0.599 | 1.59/1.15 | 152/140 | 63.5/88.3 | $2.99\times10^{-3}$ | 0.0199 |
| | | (−10.5) | | (+39.2) | | | (−27.7) | (−7.89) | (+39.1) | | |
| 40.00 | 87.48 | 0.166/0.145 | 0.0577 | $2.28\times10^{-2}/2.92\times10^{-2}$ | $2.78\times10^{-3}$ | 0.692 | 1.51/1.15 | 157/140 | 71.5/91.5 | $2.51\times10^{-3}$ | 0.0237 |
| | | (−12.7) | | (+28.0) | | | (−23.8) | (−10.8) | (+28.2) | | |
| 46.00 | 79.29 | 0.187/0.158 | 0.0513 | $1.27\times10^{-2}/1.65\times10^{-2}$ | $1.87\times10^{-3}$ | 0.762 | 1.54/1.15 | 163/142 | 72.8/94.6 | $1.54\times10^{-3}$ | 0.0337 |
| | | (−15.5) | | (+29.9) | | | (−25.3) | (−12.9) | (+29.9) | | |
| 52.00 | 70.43 | 0.225/0.184 | 0.0432 | $5.61\times10^{-3}/6.88\times10^{-3}$ | $6.41\times10^{-4}$ | 0.920 | 1.50/1.20 | 165/145 | 81.1/99.4 | $6.94\times10^{-4}$ | 0.0480 |
| | | (−21.9) | | (+22.7) | | | (−20.0) | (−12.1) | (+22.6) | | |
| 55.00 | 64.27 | 0.287/0.191 | 0.0342 | $1.71\times10^{-3}/2.05\times10^{-3}$ | $1.97\times10^{-4}$ | 1.19 | 1.52/1.20 | 172/151 | 83.6/99.9 | $3.24\times10^{-4}$ | 0.0539 |
| | | (−33.4) | | (+19.8) | | | (−21.1) | (−12.2) | (+19.5) | | |
| 56.50 | 61.62 | 0.347/0.203 | 0.0284 | $7.32\times10^{-4}/8.04\times10^{-4}$ | $9.19\times10^{-5}$ | 1.43 | 1.53/1.25 | 174/158 | 92.8/101.9 | $1.67\times10^{-4}$ | 0.0615 |
| | | (−41.4) | | (+9.84) | | | (−18.3) | (−9.20) | (+9.81) | | |
| 57.40 | 59.67 | 0.455/0.211 | 0.0218 | $1.96\times10^{-4}/2.23\times10^{-4}$ | $3.16\times10^{-5}$ | 1.85 | 1.55/1.40 | 176/182 | 95.9/111.3 | $5.77\times10^{-5}$ | 0.0705 |
| | | (−53.6) | | (+16.0) | | | (−9.68) | (+3.41) | (+16.1) | | |

Notes: experimental-tube inner-diameter = 1.640 cm, outer diameter = 1.889 cm; $r_w$ = heating-wire radius = 0.01016 cm; /, experimental *vs.* theoretically (numerically) calculated values; *, numerically calculated values; (±), deviation, in percentage, of numerically calculated values with respect to experimental values; $\Delta r = r_{max} - r_{min}$, where $r_{max}$ and $r_{min}$ are the radii of the peak and the valley respectively of the helical wave; $k = 2\pi/(\lambda/\bar{L}) \equiv$ dimensionless wavenumber; $Q = A\bar{\sigma}_i\bar{L}^2/\nu$ (dimensionless parameter); $v = \bar{\sigma}_i\lambda/2\pi \equiv$ wave speed.

TABLE 2. Summary of experimental results and theoretical calculations

(5) We also found that the dimensionless parameter $Q = A\bar{\sigma}_i \bar{L}^2/\nu$ is a weakly varying function of $\bar{L}$. As a matter of fact, the relative constancy of $Q^*$ leads to the theoretical prediction that $\bar{\sigma}_i$ is proportional to $\bar{L}^{-5}$, since $A$ is proportional to $\bar{L}^3$. The experimental $Q$-values are systematically somewhat smaller than those calculated theoretically, because the experimental values of $\bar{\sigma}_i$ are smaller than the calculated ones.

(6) Two determinations of $\bar{L}$ are also compared. Calculated values were obtained by assuming a laminar flow in the melt such that (*a*) no radial convection occurs, and (*b*) heat is transferred radially only through conduction. The measured values for the bath temperature (with a correction for heat transfer in the glass) and the wire temperature then permit a value of $\bar{L}$ to be computed. These calculated values $\bar{L}^*$ are systematically smaller than the measured experimental values $\bar{L}$. This difference becomes greater as the gap becomes larger, and reaches a factor of two at $\bar{L} = 0.455$ cm (as the bath temperature approaches the melting point of SCN). Under supercritical conditions, of course, lateral heat transport by convection becomes effective, and approximate values of $\bar{L}$ based on the unperturbed solutions need not be accurate if the convective heat transport becomes comparable to that due to conduction.

## 5. Conclusions

Experiments and linear stability analysis were carried out to characterize the effects of convective flow on the crystal–melt interface. Theory has predicted and experiment has demonstrated an interface instability under conditions for which, in the absence of flow, the solid–melt interface would be morphologically stable. Two distinct modes were observed. In the case that the Grashof number is smaller than some critical value, the interface is stable to perturbations and remains cylindrical with the flow axisymmetric. However, in the case that the Grashof number is larger than a certain critical value, the interface is unstable to perturbations and becomes helical and the flow becomes non-axisymmetric. The helical interface was observed, moreover, to rotate with a period ranging from a few minutes to more than ten hours, depending on the radial gap of the liquid region.

The observed critical Grashof numbers for our system with the deformable crystal–melt interface are an order of magnitude smaller than those predicted by Choi & Korpela (1981) and Shaaban & Özisik (1982) for systems with rigid walls. Comparison between experimental data and linear perturbation analysis shows a general agreement in both the magnitudes and scalings of various parameters.

This work was conducted under the support of the Materials Processing in Space Program, National Aeronautics and Space Administration, with liaison through the Marshall Space Flight Center (MSFC) and the Lewis Research Center (LeRC) under NASA grant NAG 3-333.

## REFERENCES

CARRUTHERS, J. R. 1977 In *Preparation and Properties of Solid State Materials*, vol. 3 (ed. W. R. Wilcox & R. A. Lefever), p. 1. Dekker.

CHOI, I. G. & KORPELA, S. A. 1980 *J. Fluid Mech.* **99**, 725.

CORIELL, S. R., BOISVERT, R. F., MICKALONIS, J. I. & GLICKSMAN, M. E. 1983 *Adv. Space Res.* (*Proc. 24th COSPAR Meeting*) **3**, 95.

CORIELL, S. R., CORDES, M. R., BOETTINGER, W. J. & SEKERKA, R. F. 1980 *J. Crystal Growth* **49**, 13.

CORIELL, S. R. & SEKERKA, R. F. 1981 *Physico-Chem. Hydrodyn.* **2**, 281.

DELVES, R. T. 1974 In *Crystal Growth*, vol. 1 (ed. B. R. Pamplin), p. 40. Pergamon.

DRAZIN, P. G. & REID, W. H. 1981 *Hydrodynamic Stability*. Cambridge University Press.

FANG, Q. T. 1983 M. S. thesis, Materials Engineering Department, Rensselaer Polytechnic Institute.

GARG, V. K. 1981 *J. Fluid Mech.* **110**, 209.

GLICKSMAN, M. E. & MICKALONIS, J. I. 1982 In *Proc. 16th Southeastern Seminar on Thermal Science, Miami, Florida*, vol. 1, p. 505.

GLICKSMAN, M. E., SCHAEFER, R. J. & AYERS, J. D. 1976 *Metall. Trans.* **7A**, 1747.

HURLE, D. T. J. 1977 In *Current Topics in Materials Science*, vol. 2 (ed. E. Kaldis & H. J. Scheel), p. 549. North-Holland.

LANGER, J. S. 1980 *Rev. Mod. Phys.* **52**, 1.

MICKALONIS, J. I. 1982 M.S. thesis, Materials Engineering Department, Rensselaer Polytechnic Institute.

MULLINS, W. W. 1963 In *Metal Surfaces*, chap. 2. Am. Soc. Metals, Metal Park, Ohio.

PIMPUTKAR, S. M. & OSTRACH, S. 1981 *J. Crystal Growth* **55**, 614.

POWELL, M. J. D. 1970 In *Numerical Methods for Nonlinear Algebraic Equations* (ed. P. Rabinowitz). Gordon & Breach.

SCHAEFER, R. J., GLICKSMAN, M. E. & AYERS, J. D. 1975 *Phil. Mag.* **32**, 725.

SCOTT, M. R. & WATTS, H. A. 1977 *SIAM J. Numer. Anal.* **14**, 40.

SHAABAN, A. H. & ÖZISIK, M. N. 1982 In *Proc. 7th Intl Heat Transfer Conf., Munich*, vol. 2, p. 281.

WOLLKIND, D. J. 1979 In *Preparation and Properties of Solid State Materials*, vol. 4 (ed. W. R. Wilcox), p. 111. Dekker.